Petroleum Science 23 (2026) 1319–1334

Contents lists available at ScienceDirect

Petroleum Science

journal homepage: www.keaipublishing.com/en/journals/petroleum-science

Original Paper

Dual-modality microwave-conductivity sensing system for flow characterization in high water-cut production wells

Lan-Di Bai, Ning-De Jin *, Chuan-Shun Liu, Ji-Dong Wei, Ying-Yu Ren

School of Electrical and Information Engineering, Tianjin University, Tianjin, 300072, China

ARTICLE INFO

Article history:
Received 15 May 2025
Received in revised form
2 December 2025
Accepted 3 December 2025
Available online 9 December 2025

Edited by Jia-Jia Fei

Keywords:
Liquid-liquid flows
Flexible microstrip array antenna
Conductance sensor
Water holdup
Superficial velocity

ABSTRACT

This study introduces a novel microwave-conductivity dual-modality sensing system for liquid-liquid flow measurement in oilfield water injection. The system combines a flexible microstrip array antenna (FMAA) for water holdup detection and multi-height electrode conductance sensors (CSMHEs) for cross-correlation velocity measurement. The microstrip array design of the FMAA ensures a more uniform electric field distribution, effectively mitigating the influence of nonuniform flow structures. The geometric dimensions of the FMAA are meticulously optimized through finite element analysis. Simulation reveals that the phase output exhibits high sensitivity to water holdup at 1.3 GHz. Dynamic oil-water flow experiments are conducted. The identification of four distinct flow patterns was achieved by analyzing real-time snapshots and synchronized output signals from both the FMAA and CSMHEs. Water holdup is determined by establishing mixed dielectric constant models for different flow patterns using the FMAA. The results indicate a strong correlation between the phase outputs of the FMAA and the water holdup, with a measurement error of 2.27%. Furthermore, a relationship was established between the cross-correlation velocity obtained from the CSMHEs and the mixture and oil superficial velocities. Additionally, by establishing drift-flux models for different flow patterns, the relationships among oil superficial velocity, water holdup, and mixture velocity are determined. Through the simultaneous solution, the prediction of mixture velocity and phase superficial velocities is ultimately achieved. The measurement error of superficial velocities of water and oil are 3.44% and 19.12%, respectively. This approach demonstrates an effective new methodology for measuring liquid-liquid flows.

1. Introduction

Liquid-liquid flows are prevalent in petroleum industry operations. Among these, accurate measurement of oil-water two-phase flow parameters is critical for characterizing dynamic production behavior. As waterflooding techniques advance, middle-late oilfields increasingly exhibit oil-in-water flow. The complex phase interactions and pronounced slippage effects create intricate flow patterns, posing significant challenges for parameter acquisition in production profile logging.

Due to the significant differences in physical properties such as conductivity and dielectric constant between oil and water, various water content measurement techniques have been developed, including conductance, capacitance, and microwave methods (Chen et al., 2017; Jia et al., 2024; Karimi et al., 2018). Demori et al. (2010) proposed a solution for capacitive sensing in the presence of conductive water by increasing the operating frequency to 2 MHz. The microwave method utilizes high-frequency electromagnetic waves, whose propagation characteristics are directly influenced by the medium's dielectric properties. Microwave sensing has been widely employed in microfluidics (Sorocki et al., 2020), geofluid characterization (Alvarez, 2018), and soil moisture detection (Amiri et al., 2023). Due to its non-invasive nature, full-scale measurement capability (0–100%), and real-time monitoring potential, microwave sensors are increasingly being adopted for water holdup measurement in multiphase flow. Common microwave measurement techniques include resonance,

* Corresponding author.
E-mail address: ndjin@tju.edu.cn (N.-D. Jin).
Peer review under the responsibility of China University of Petroleum (Beijing).

https://doi.org/10.1016/j.petsci.2025.12.006

transmission, and reflection methods (Kongkeaw et al., 2025; Yang et al., 2021; Sabzevari et al., 2020). While the resonance method offers high sensitivity, its application is primarily limited to single-phase fluids or homogeneous mixtures (Kamal et al., 2024). In non-uniform flows, the resonance characteristics become susceptible to flow structure variations, resulting in multiple ambiguous resonance points that are challenging to accurately identify and interpret. Unlike resonance approach, transmission and reflection methods enable continuous real-time monitoring at a fixed frequency by analyzing phase and amplitude variations in microwave signals (Zhao et al., 2019; Lin et al., 2020). This characteristic makes them particularly suitable for measuring non-uniform fluid systems. Microstrip antennas, valued for their compact design, affordability, and conformal properties, are finding growing use in water content measurement. Various implementations have been demonstrated, including three-antenna microwave sensors (Bo and Nyfors, 2002), leaky-wave antennas (Shen et al., 2022), and specialized microstrip antenna sensors (Ghretli et al., 2007; Sattari and Hayati, 2024). Further developments have been reported by Wei et al. (2019), Wang et al. (2021), and Xue et al. (2020). These flat-type microwave sensors are typically installed either externally on the measurement pipeline (making downhole fluid measurements difficult to implement) or inserted directly into the measured fluid for localized detection-an approach that not only disturbs the flow field but also demonstrates significant limitations when measuring fluids with complex flow patterns. The advancement of flexible PCB technology has further enabled the fabrication of conformal microwave sensors for pipeline applications (Deif and Daneshmand, 2020; Hossein et al., 2018; Olokede et al., 2021), particularly for detecting water ingress, coating delamination, dynamic uniform flows, and microfluidic systems. While existing studies have successfully addressed water content measurement in well-defined flow conditions or static mixtures, extending these microwave techniques to complex, dynamic flow conditions continues to present significant technical challenges.

Conventional approaches to measuring flow velocity in multiphase systems typically utilize turbine flowmeters, electromagnetic flowmeters, and Venturi flowmeters (Gupta et al., 2016; Li et al., 2009; Lin et al., 2020; Tang et al., 2022). During long-term waterflood development in onshore oilfields, the conductance cross-correlation technique has emerged as an effective method for measuring velocity in water-continuous oil-water flows (Beck, 1981). Various sensor configurations have been developed for this purpose, including multichannel conductance probes (Barnea et al., 1980; Han et al., 2017), multi-sector arrays (Costigan and Whalley, 1997; Bai et al., 2021), and ring-type sensors (Asali et al., 1985; Fossa, 1998). Annular conductance sensors have proven particularly valuable for analyzing fluid concentration distributions across pipe cross-sections. Significant contributions to this field include: Ring conductance sensors developed by Asali et al. and Fossa (Asali et al., 1985; Fossa, 1998); An impedance-based method using dual ring electrodes proposed by Andreussi et al. (1988); Subsequent improvements to conductance ring technology by Lucas et al. (2000), Devia and Fossa (2003), Wang et al. (2019), and Zhai et al. (2012). Our investigation demonstrates that the accuracy of cross-correlation velocity measurement is critically determined by two interdependent factors: the spatial coverage and distribution uniformity of the sensor's sensitive field, alongside the transient coupling effects arising from the interaction between the dispersed phase and the sensitive field. Consequently, the development of velocity sensors featuring both high sensitivity and uniform field distribution represents a crucial research direction for accurately characterizing multiphase flow with complex flow patterns.

This study presents an investigation of oil-water two-phase flow using the newly designed flexible microstrip array antenna (FMAA) and the CSMHEs. The developed CSMHEs demonstrate the capability to effectively capture the propagation characteristics of global average kinematic waves, building upon their previously validated performance in gas-liquid flow (Liu et al., 2022). In this study, we propose to extend this technique to liquid-liquid flow velocity characterization. The study protocol encompassed the development and geometric optimization of the FMAA model with subsequent water holdup validation. This was followed by dynamic experiments utilizing real-time monitoring to identify four distinct flow patterns: dispersed oil-in-water (D O/W), dispersed oil-in-water slug (D OS/W), very fine dispersed oil-in-water (VFD O/W), and transition flow (TF). Further steps included the establishment of flow pattern-specific dielectric models for water holdup determination, velocity correlation measurements based on CSMHE sensors, and the application of drift-flux models to predict phase velocities by incorporating flow pattern effects.

2. Flexible microwave array antenna

2.1. Structure design

As illustrated in Fig. 1, the FMAA structure is composed of three key components: an array antenna, coaxial feeders, and a shield

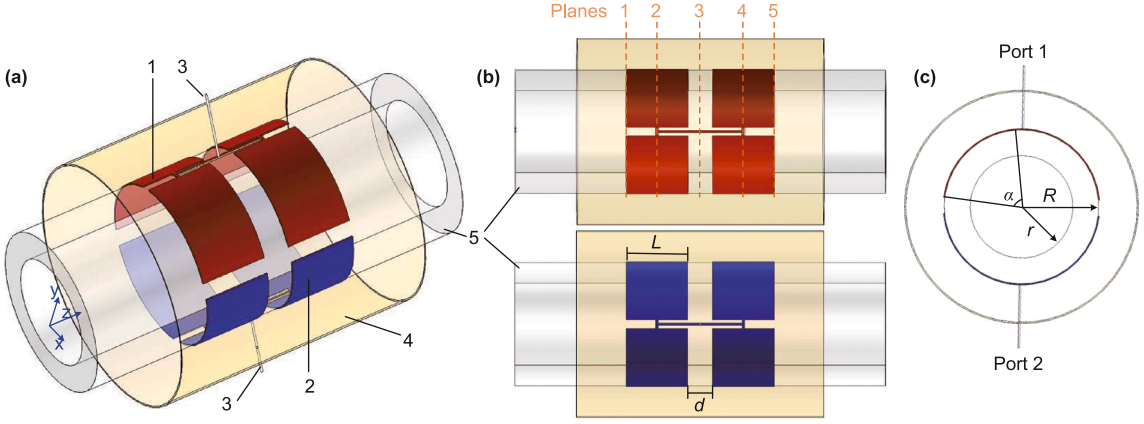

Fig. 1. Structural configuration of the FMAA: (**a**) 3D schematic highlighting conformal mounting on PMMA pipe; (**b**) Top/bottom views of symmetrical rectangular patches; (**c**) Side profile illustrating coaxial feedlines and shield layer (GND) integration.
1. Exciting patch; 2. Receiving patch; 3. Coaxial feeder; 4. Shield layer; 5. Pipe.

layer. The array antenna incorporates both exciting and receiving patches, each designed with four geometrically symmetrical rectangular elements. These elements are fabricated from flexible PCB material with 1 oz (35 μm) rolled copper cladding, supported by a 0.2 mm thick dielectric substrate. The FMAA is externally mounted on a PMMA (polymethyl methacrylate) pipe with 10 mm inner radius (r) and 15 mm outer radius (R), enabling non-intrusive measurements. The antenna patches are fully enclosed by a copper shielding layer (GND) that simultaneously confines electromagnetic wave propagation into pipe and protects against external electromagnetic interference. The FMAA's optimization parameters include the length of each plate L, the plate angle α and the plate spacing d. The array antenna structure configuration enhances EM field uniformity within the pipe, thereby minimizing flow structure influence.

Water, being a polar solvent, exhibits a substantially higher dielectric constant than nonpolar oil solvents. Its frequency-dependent dielectric properties obey the Debye relation:

$$\varepsilon_{\mathrm{wr}} = \varepsilon'_{\mathrm{w}\infty} + \frac{\varepsilon'_{\mathrm{ws}} - \varepsilon'_{\mathrm{w}\infty}}{1 + j2\pi f\tau} - j\frac{\sigma}{2\pi f\varepsilon_0} = \varepsilon'_{\mathrm{wr}} - j\left(\varepsilon''_{\mathrm{wd}} + \frac{\sigma}{2\pi f\varepsilon_0}\right) \tag{1}$$

where $\varepsilon_{\mathrm{wr}}$ is the relative dielectric constant, $\varepsilon'_{\mathrm{w}\infty}$ is the high-frequency dielectric constant, $\varepsilon'_{\mathrm{ws}}$ is the static dielectric constant, $\varepsilon'_{\mathrm{wr}}$ is the real part of the water dielectric constant, $\varepsilon''_{\mathrm{wd}}$ is the dielectric loss, ε_0 is the dielectric constant in a vacuum, f is the working frequency, τ is the relaxation time, and σ is the conductivity determined by water salinity. The $\varepsilon''_{\mathrm{wd}}$ and τ are influenced by temperature. In this experiment, we studied a mixture of tap water (salinity: 180 ppm) and oil at a fixed working frequency under room temperature conditions. Based on Eq. (1), the real part of water's dielectric constant remains stable (~78 at microwave frequencies) (Kestin et al., 1978). The oil dielectric constant is 3.2.

Given the significant contrast in dielectric properties between water and oil, the dielectric constant of an oil-water mixture depends on the phase fraction, altering the microwave field's wave vector and consequently impacting the transmission coefficient S_{21}. While several mixed dielectric constant models have been proposed based on phase distribution (Sheen et al., 2010; Bruggeman, 1935), their applicability remains constrained in complex flow patterns due to inaccuracies in water holdup estimation. At a fix frequency, the mixture dielectric constant can be theoretically expressed as:

$$\varepsilon_{\mathrm{m}} = \varepsilon_{\mathrm{m}}(Y_{\mathrm{w}}, \varepsilon_{\mathrm{o}}, \varepsilon_{\mathrm{w}}) = F(Y_{\mathrm{w}}) \tag{2}$$

where ε_{o} and ε_{w} denote the dielectric constants of oil and water, respectively. And Y_{w} represents the water holdup (i.e., the water content in cross-section).

As the microwave signal propagates through the test material between the transmitting and receiving antennas, the resulting phase shift $\Delta\theta$ relates to the material's dielectric constant ε_{m} through:

$$\Delta\theta = \frac{2\pi d}{\lambda_0}\left(\sqrt{\varepsilon'_{\mathrm{m}}} - 1\right) \tag{3}$$

where λ_0 is the free space wavelength, d is the thickness of the measured material. The real part of the dielectric constant of the material can be expressed:

$$\varepsilon'_{\mathrm{m}} = \left(\frac{\lambda_0}{2\pi d}\Delta\theta + 1\right)^2 \tag{4}$$

The microwave phase shift thus provides a direct measure of the mixture dielectric constant, allowing determination of the oil-water two-phase flow's dielectric properties across all working conditions.

2.2. Optimization and simulation

The variation of mixture dielectric constant not only affects the phase shift, but also is related to the working frequency. We selected 1.3 GHz (L-band) to ensure adequate field coverage while meeting circuit design and signal transmission constraints. The microwave response of the FMAA was numerically analyzed using Ansys HFSS 2019 (high frequency structure simulator), a full-wave 3D electromagnetic field simulation tool based on finite element method (FEM). The field properties of the electromagnetic field formed by microwave sensors can be described by the Helmholtz equation (Li et al., 2006):

$$\vec{J} = \nabla \times \vec{H} - j\omega\varepsilon\vec{E} \tag{5}$$

$$\vec{M} = -\nabla \times \vec{E} - j\omega\mu\vec{H} \tag{6}$$

where E denotes the electric field strength (unit: V/m), H represents the magnetic field intensity (unit: A/m), J is the electric current density (unit: A/m^2), M stands for the equivalent magnetic current density (unit: V/m^2), and μ corresponds to the magnetic permeability (unit: H/m).

For a three-dimensional spatial domain Ω, let its boundary surface be Γ. The vector boundary equation of the electromagnetic field obtained by the weighted residual method is as follows (Chen et al., 2001):

$$\frac{\omega_i}{4\pi}\vec{H_i}(\vec{r}) = -\oint_D \left\{ \begin{array}{l} \mathrm{j}\omega\varepsilon\vec{n} \times \vec{E}(\vec{r'})G(\vec{r}, \vec{r'}) + \\ \vec{n} \times \vec{H}(\vec{r}) \times \nabla G(\vec{r}, \vec{r'}) + \\ \vec{n}\vec{H}(\vec{r'})\nabla G(\vec{r}, \vec{r'}) \end{array} \right\} \mathrm{d}\Gamma(\vec{r'}) \tag{7}$$

where $\vec{n}$ represents the outward normal unit vector of Γ, vector $\vec{r}$ describes the displacement from source (x', y', z') to field point (x, y, z). The ω_i represents the solid angle stretched at point i, and $G(\vec{r}, \vec{r'})$ represents the fundamental solution of the three-dimensional Helmholtz equation. Region Ω (occupied by the dielectric layer) is discretized into M_1 triangular elements, while boundary Γ is partitioned into M_s linear segments. Given N nodes within Ω, an interpolation procedure is applied to each element, followed by summation over the entire domain. The partial derivatives of the field quantities at each node are then evaluated, and the global assembly yields the boundary conditions at the dielectric interface.

Fig. 2 shows the equivalent circuit of the designed two-port network. With microwave excitation at Port 1 ($\overline{U_1}^+$), normalized output voltages ($\overline{U_1}^-$ and $\overline{U_2}^-$) appear at both ports, following the ***S***-parameter relationship:

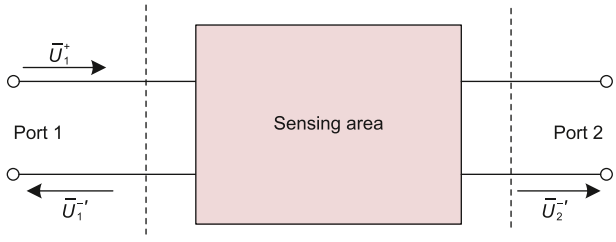

Fig. 2. ***S***-parameter characterization of the FMAA two-port network at 1.3 GHz.

$$\begin{bmatrix} \overline{U_1}^{'} \\ \overline{U_2}^{'} \end{bmatrix} = \boldsymbol{S} \cdot \overline{U_1}^{+} = \begin{bmatrix} S_{11} \\ S_{21} \end{bmatrix} \cdot \overline{U_1}^{+} \tag{8}$$

In the microwave sensing, the $\boldsymbol{S}$ parameter is affected by the impedance, there is:

$$\boldsymbol{S} = (\overline{\boldsymbol{Z}} - \boldsymbol{M})(\overline{\boldsymbol{Z}} + \boldsymbol{M})^{-1} \tag{9}$$

where $\boldsymbol{M}$ is the identity matrix, $\boldsymbol{Z}$ is the impedance parameter, which is depended by the characteristic impedance of the FMAA, the coaxial feeder and the equivalent impedance of the oil-water mixture. By analyzing the phase output of the transmission coefficient S_{21}, the water holdup can be measured.

The two coaxial feeders are designated as excitation ports, configured as wave ports with a characteristic impedance (Z_o) of 50 Ω to minimize impedance mismatch losses with the measurement system. In addition to Z_o, the characteristic impedance (Z_1) of the array antenna also influences the detection performance of the FMAA. The methodology proceeds as follows: First, we establish the reference phase value (S_w) using tap water as the baseline medium. Subsequently, a 1 mm oil droplet is introduced into the FMAA measurement area and systematically positioned at 262 discrete locations within each of five cross-sectional planes. The five selected cross-sectional planes are uniformly distributed along this axial direction to cover and evaluate the electromagnetic field characteristics of the entire sensitive region between the antennas as shown in Fig. 1(b). Plane 1 and Plane 5 are positioned immediately outside the outer edges of the exciting patch and receiving patch, respectively, to assess the field characteristics at the antenna fringes. Plane 2 and Plane 4 are located at the center of the exciting patch and receiving patch, respectively. And Plane 3 is precisely at the midpoint between the exciting and receiving patches. This distribution allows for a systematic evaluation of the uniformity and sensitivity of the sensitive field throughout the entire axial range between the antennas. And the distribution of the 262 discrete locations in each cross-sectional plane is shown in Fig. 3. Each pipe cross-section is treated as a circular area with a radius of 10 mm. A uniform polar coordinate grid was established within this circular area. And points are placed at equal intervals along the radial direction, and distributed uniformly in the circumferential (angular) direction. Any grid points falling outside the pipe wall (i.e., outside the circular boundary) are automatically filtered out. Using this method, we obtained a largely consistent number of uniformly distributed spatial points on each plane.

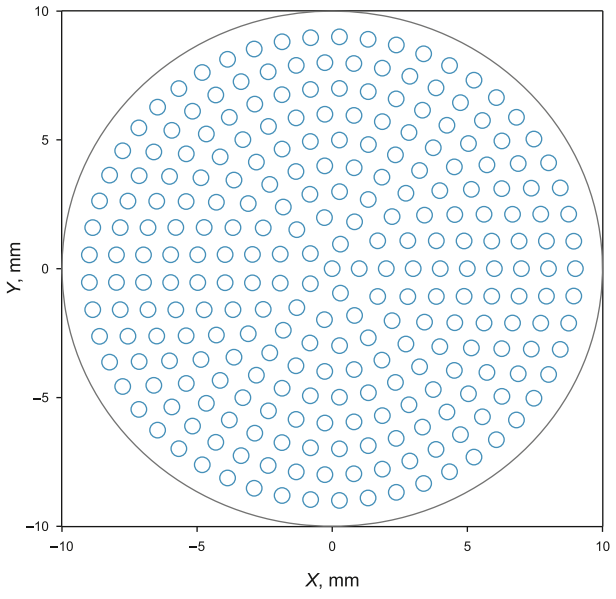

Fig. 3. Sensitivity mapping of oil droplet positions (d = 1 mm) within five cross-sectional planes of the FMAA measurement region.

At each position, the resulting phase output (S) is recorded, enabling calculation of the phase variation induced by the oil droplet's presence:

$$\Delta S_{21}(x,y,z) = S - S_w \tag{10}$$

Therefore, the sensitivity parameter of the FMAA can be expressed as:

$$S(x,y,z) = \Delta S_{21}(x,y,z) \,/\, [\Delta S_{21}(x,y,z)]_{max} \tag{11}$$

The average sensitivity S_{avg} of the FMAA caused by 262 oil droplets is calculated as:

$$S_{avg} = \sum_{j=1}^{262} S_j \Big/ 262 \tag{12}$$

where S_j is the sensitivity value corresponding to the j-th oil droplet.

The SVP (sensitivity variation parameter) is the ratio of the sensitivity standard deviation to the sensitivity average:

$$SVP = \frac{S_{dev}}{S_{avg}} \times 100\% \tag{13}$$

where S_{dev} represents the standard deviation of sensitivity at each spatial position traversed by the oil droplet:

$$S_{dev} = \left(\frac{1}{262} \sum_{j=1}^{262} \left(S_j - S_{avg} \right)^2 \right)^{1/2} \tag{14}$$

A higher S_{avg} signifies that the FMAA exhibits greater responsiveness to minute variations, while a smaller SVP indicates improved field uniformity across the measurement region to a more uniform spatial sensitivity distribution across the measurement region.

The sensor dimensions are optimized based on the experimental pipe diameter and observed flow patterns. In the initial optimization phase, we fix the values of L and d as 10 and 3 mm respectively, while systematically varying the α from 60° to 85° in 5° increments. As shown in Table 1, the optimal performance was achieved at α = 80°, where the S_{avg} reached its maximum value while the SVP was minimized. The corresponding sensitivity field distributions for different plate angles are presented in Fig. 4. The α = 80° configuration demonstrates both enhanced sensitivity magnitude and superior uniformity in the sensitivity field distribution compared to other angles.

Following the determination of the optimal plate angle (α = 80°) and fixed electrode spacing (d = 3 mm), we

Table 1
The s_{avg} and the SVP at different α

α	L, mm	d, mm	S_{avg}	SVP
60°	10	3	0.1865	0.7016
65°	10	3	0.2548	0.5808
70°	10	3	0.5915	0.3150
75°	10	3	0.1881	1
80°	**10**	**3**	**0.6119**	**0.1626**
85°	10	3	0.3212	0.8102

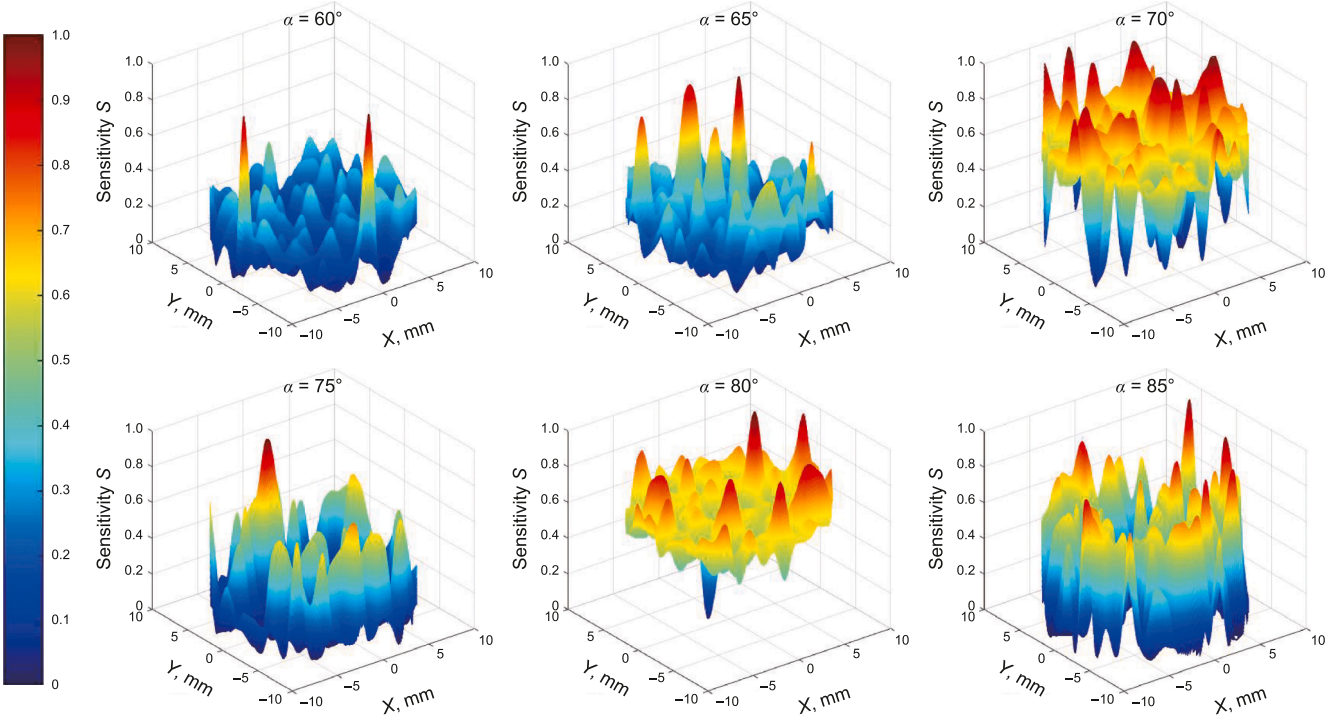

Fig. 4. Sensitivity field distribution of the FMAA under varying plate angle.

Table 2
The s_{avg} and the SVP at different L.

α	L, mm	d, mm	S_{avg}	SVP
80°	7	3	0.3161	0.7225
80°	8	3	0.4842	0.4269
80°	9	3	0.2527	0.5991
80°	**10**	**3**	**0.6118**	**0.1626**
80°	11	3	0.2841	0.7633
80°	12	3	0.5298	0.4747

systematically optimized the plate length (L) across a range of 7–12 mm. The results demonstrate that $L = 10$ mm yields both the maximum S_{avg} and minimum SVP (Table 2), indicating optimal sensor performance. This finding is further supported by the sensitivity field distributions shown in Fig. 5, where the $L = 10$ mm configuration exhibits the highest sensitivity magnitude while maintaining excellent field uniformity.

Finally, we optimized the plate spacing (d) while maintaining the previously determined optimal parameters ($\alpha = 80°$, $L = 10$ mm). Table 3 presents the S_{avg} and the SVP as functions of d. The results demonstrate that $d = 3$ mm yields both the maximum S_{avg} and minimum SVP, indicating optimal sensor performance. Fig. 6 illustrates the sensitivity field distributions for different plate spacings under these fixed conditions. The $d = 3$ mm configuration exhibits not only enhanced sensitivity magnitude but also superior field uniformity compared to other spacings. Through comprehensive parametric optimization, we conclude that the geometric configuration with $\alpha = 80°$, $L = 10$ mm, and $d = 3$ mm represents the optimal design for the FMAA sensor, achieving the best balance between sensitivity and uniformity.

The preceding simulations characterize the output response of the FMAA to oil droplets at various spatial positions. Subsequently, we investigate the phase response of the FMAA under varying water holdup conditions. This response is quantified as the sensor's sensitivity (δ), defined as the ratio of phase shift to water holdup change:

$$\delta = \frac{\Delta\theta}{\Delta Y_w} \tag{15}$$

In our simulations, we systematically investigated the FMAA's response across a water holdup (Y_w) range of 0.5–0.9 with 0.05 increments. The relative dielectric constants are set as $\varepsilon_o = 3.2$ for oil and $\varepsilon_w = 78$ for water. Fig. 7 presents the resulting phase output variations versus water holdup with different sizes. The results demonstrate an inverse relationship between the Y_w and phase output for a fixed size.

Fig. 7(a) ($L = 10$ mm, $d = 3$ mm): The phase output exhibits a consistent positive correlation with the α, showing comparable growth rates across all tested angles (60°–85°). Sensitivity analysis reveals stable performance with δ values of 0.16, 0.16, 0.15, 0.15, and 0.14 deg/%Y_w respectively. Fig. 7(b) ($\alpha = 80°$, $d = 3$ mm): Phase output demonstrates an inverse relationship with the L. Notably at $L = 7$ mm, anomalous negative phase outputs occur within $Y_w = 0.5$–0.6, indicating measurement nonlinearity in this configuration. Sensitivity gradually decreases from 0.18 to 0.13 deg/%Y_w as L increases from 8 to 12 mm. Fig. 7(c) ($\alpha = 80°$, $L = 10$ mm): Increasing d leads to reduced phase output, with comparable decay rates observed across all sizes (2–6 mm). The corresponding sensitivity values show a mild decline from 0.16 to 0.13 deg/%Y_w.

The parametric analysis reveals three key findings regarding the FMAA's geometric optimization. First, the plate length L exhibits the most significant impact on phase output among the three geometric parameters (α, d, L), attributed to the expanded coverage area of exciting/receiving plates in longer microstrip antennas, which substantially modifies microwave transmission characteristics. Second, while all parameters influence phase output, their sensitivity coefficients (δ) vary minimally, with the configuration $\alpha = 80°$, $L = 10$ mm, and $d = 3$ mm demonstrating optimal sensitivity performance ($\delta = 0.15$ deg/%Y_w). Finally,

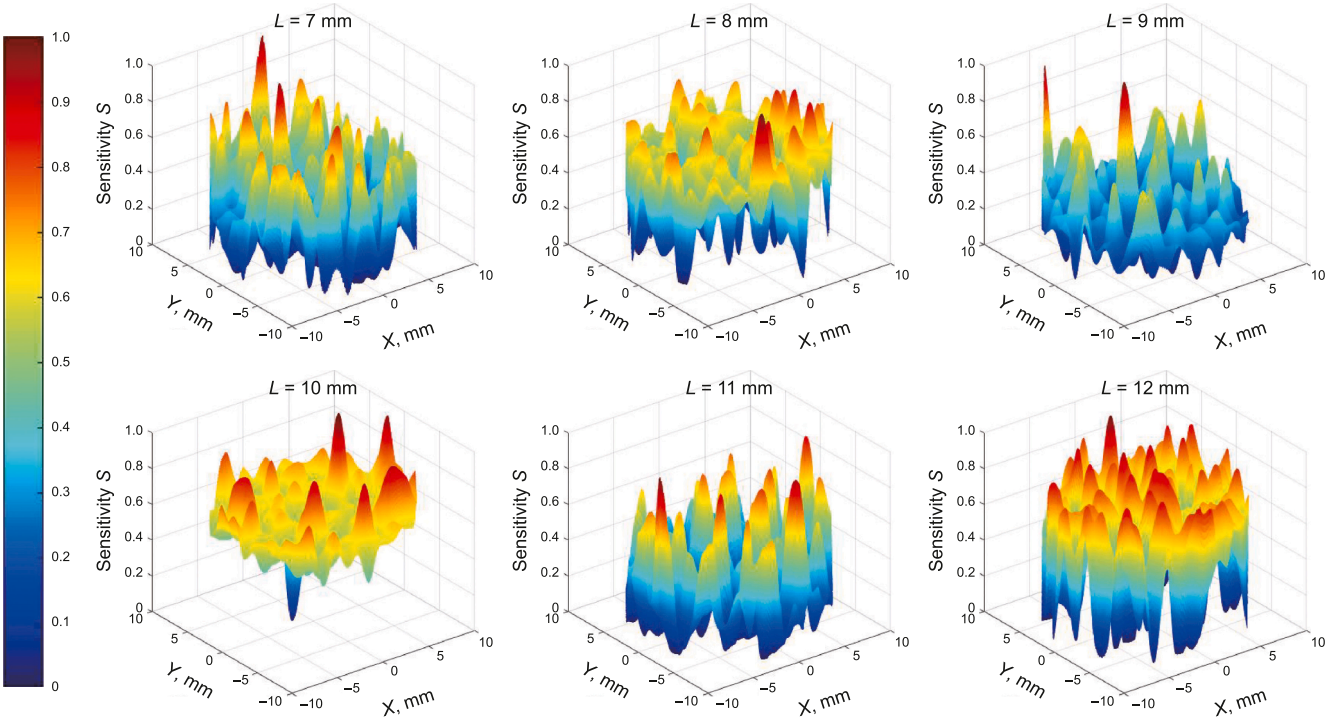

Fig. 5. Sensitivity field distribution of the FMAA under varying plate length.

Table 3
The s_{avg} and the SVP at different d.

α	L, mm	d, mm	S_{avg}	SVP
80°	10	2	0.1196	1.1610
80°	**10**	**3**	**0.6119**	**0.1626**
80°	10	4	0.2425	0.8768
80°	10	5	0.1293	1.2208
80°	10	6	0.1223	0.8092

evaluations of S_{avg} and SVP under non-uniform oil-water distributions confirm the robustness of this optimized geometry, validated through comprehensive sensitivity metrics and field distribution analysis.

3. Dynamic experiment

3.1. Experimental setup

Based on the optimization results, we fabricated the FMAA prototype (Fig. 8) through the following manufacturing process: (1) Patch preparation: Flexible exciting and receiving patches are laser-cut from copper-clad polyimide film. (2) Patch installation: The patches are precisely aligned and bonded symmetrically to the pipe's outer surface using high-temperature epoxy adhesive. (3) Shielding assembly: A 0.2 mm-thick copper shield layer is formed into a cylindrical cavity, the assembly was mechanically supported by a precision-machined acrylic insulating ring. (4) Feedline connection: Two SMA connectors are soldered to the shield layer with RF-grade silver solder, the connector shells were electrically bonded to the shield layer. And the center conductors are routed through shielded feedthrough holes to connect with the patches. Then, we carry out a dynamic experiment, the two coaxial feedlines of the FMAA are respectively linked with the signal source and phase detection circuit.

Fig. 8 illustrates the dynamic experimental setup for oil-water two-phase flow. The system consists of three primary components: (1) storage tanks including separate water and oil reservoirs plus a mixing tank; (2) transparent PMMA test sections measuring 2600 mm in length with 10 mm inner diameter and 15 mm outer diameter; and (3) integrated measurement systems incorporating both the FMAA and the CSMHEs. This configuration enables comprehensive flow parameter analysis under controlled experimental conditions. Additionally, there's a set of quick closing valves (QCV) for water holdup calibration. A high-speed camera is applied to take snapshots, installed 150 cm above the entrance of the vertical pipe to ensure the fluid fully developed before measurement. The dynamic experiment is conducted at room temperature 25 °C. The continuous phase is the tap water (density is 1000 kg/m^3, viscosity is 1 mPa·s), and the dispersed phase is the No. 3 industrial white oil (density is 801 kg/m^3, viscosity is 2.8 mPa·s), belonging to Newtonian fluid. To enhance visual contrast, the oil phase was stained with Sudan red dye. Due to the significant density difference between the two phases, they remain immiscible, and no emulsification occurs under the prevailing experimental conditions. After entering the mixing tank and standing for a period, the two phases will automatically separate, with the oil phase floating on top of the water phase, forming a distinct interface. The WT600F industrial intelligent peristaltic pump are used to control velocities of oil and water, the uncertainty of them corresponds to ±0.2%, therefore, the combined uncertainty can be calculated as: $u = \sqrt{(0.2\%)^2 + (0.2\%)^2} \approx 0.28\%$.

The total flow Q_m ranges from 2 to 9 m^3/day. The mixture velocity U_m, calculated as Q_m/A (where the cross-sectional area $A = \pi r^2$ and the inner radius $r = 10$ mm), ranged from 0.073 to 0.332 m/s; the water cut K_w varied from 50% to 98%. The calculated velocities, defined as the flow rate per unit area, are determined as follows: the superficial velocity of water (U_{sw}), calculated by $U_m \times K_w$, ranges from 0.036 to 0.325 m/s, while that of oil (U_{so}),

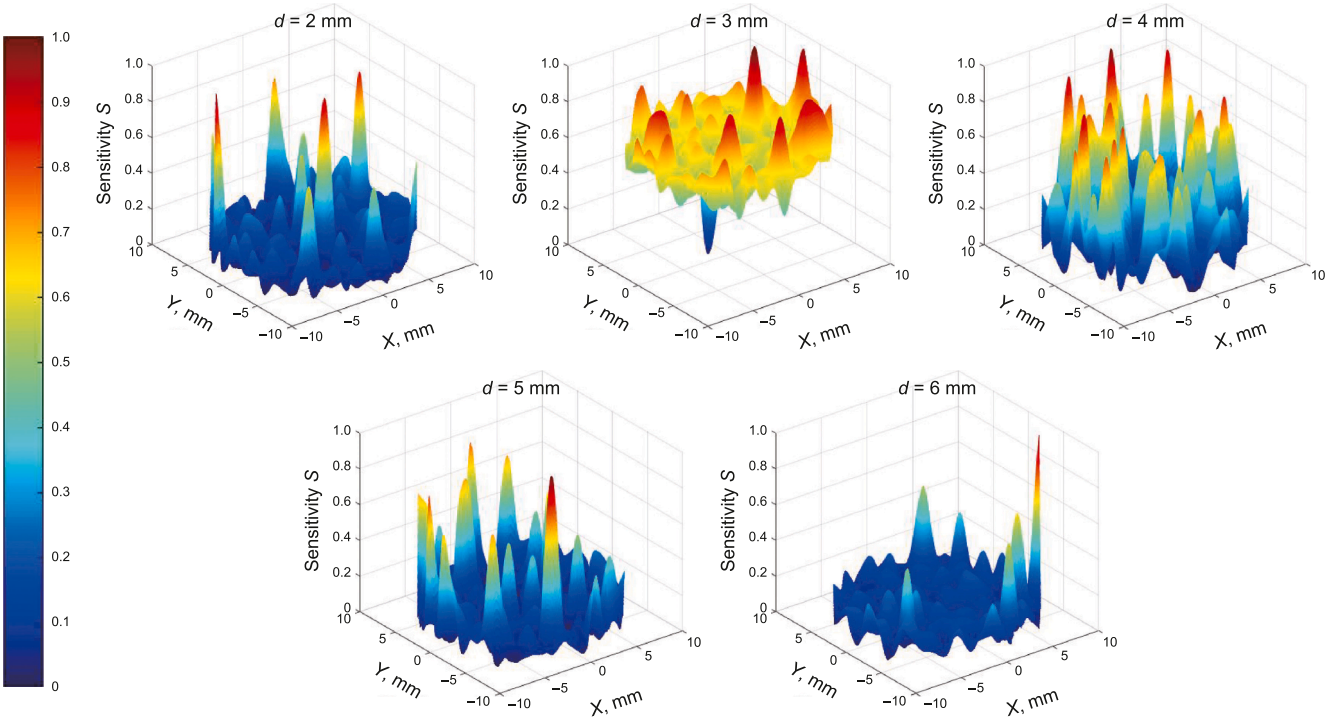

Fig. 6. Sensitivity field distribution of the FMAA under varying plate spacing.

given by $U_m - U_{sw}$, ranges from 0.001 to 0.166 m/s. The flow rates for the water phase (Q_w) and oil phase (Q_o) are derived from the total flow rate (Q_m) using the relationships $Q_w = Q_m \times K_w$ and $Q_o = Q_m - Q_w$, resulting in operational ranges of 1–8.82 m^3/day for water and 0.18–1 m^3/day for oil.

The measurement system of the FMAA includes signal source ADF4351, power splitter, phase detection circuit (key chip: AD8302), and acquisition system. The ADF4351 generates a microwave signal that is equally divided by the power splitter—one output drives the FMAA's exciting patch while the other serves as the reference signal for the AD8302 phase detector. The receiving patch's output is fed to the detector's second input port, with the resulting phase difference signals digitized by the PXI-4472 system.

The cross-correlation velocity measured using the CSMHEs, whose structure is established in Fig. 8. It comprises an exciting ring electrode (height $h = 4$ mm) mounted on the central body and a receiving ring electrode (height $H = 3$ mm) embedded in the pipe wall. Two identical conductance sensors positioned 30 mm apart (upstream/downstream) to prevent electric field interference. The detailed optimization process of the CSMHEs is described in Liu et al. (2022). The height differential between electrodes ($h > H$) creates an optimized field gradient, while the 30 mm separation ensures signal integrity. Detailed optimization procedures and performance validation are documented in Liu et al. (2022). The introduction of the center body effectively overcomes the uneven distributed oil phase.

4. Flow patterns

High-speed camera imaging reveals four distinct flow patterns (Fig. 9): three water-continuous flow patterns: D OS/W, D O/W, and VFD O/W, along with the TF. At low mixture velocities, the oil-water two-phase flow exhibits smaller turbulent kinetic energy, promoting droplet coalescence into large oil slugs (D OS/W, Fig. 9(a)). As the U_m increases, enhanced turbulence breaks these slugs into dispersed droplets, creating more chaotic flow structures (D O/W flow, Fig. 9(b)). Further mixture velocity increases produce intense shear forces that fragment droplets into micron-scale particles, establishing VFD O/W flow pattern (Fig. 9(c)). Under conditions of high U_m coupled with low K_w, the TF emerges (Fig. 9(d)), characterized by intermittent phase inversion where oil and water alternately become the continuous phase. Signals of the FMAA and the CSMHEs are presented in Fig. 10. In the D O/W flow, the signals exhibit intermittent small jumps with a uniform yet random distribution. In the D OS/W flow, the signals display quasi-periodic alternation between high and low signal levels, where the high-level fluctuations indicate dispersed oil droplets in water, while the low-level variations reveal the presence of a liquid film surrounding the oil slugs. In the VFD O/W flow, the highly uniform fluid distribution results in minimal but frequent signal fluctuations. In the TF, the signal shows non-uniform distribution, which is periodical similar to that of the D OS/W flow but the fluctuation is more volatile, and due to the increase of oil phase, the output voltage is reduced.

Weighted recurrence plot (WRP) analysis is applied to the upstream sensor's output signals from the CSMHEs for flow pattern identification. The recurrence plot was first introduced by Eckmann et al. (1987) to visualize the recurrence of trajectories to specific states in phase space, capturing fundamental characteristics of deterministic dynamical systems while also revealing the internal structure of nonlinear time series. Later, Eroglu et al. (2014) developed the weighted recurrence plot (WRP) as an extension of this methodology. The weighted recurrence plot (WRP) improves upon conventional recurrence analysis by applying an exponential transformation to the distance matrix $\mathbf{W}_{i,j} = \|x_i - x_j\|$ of the original recurrence plot (RP), thereby generating weighted recurrence values that better capture system dynamics:

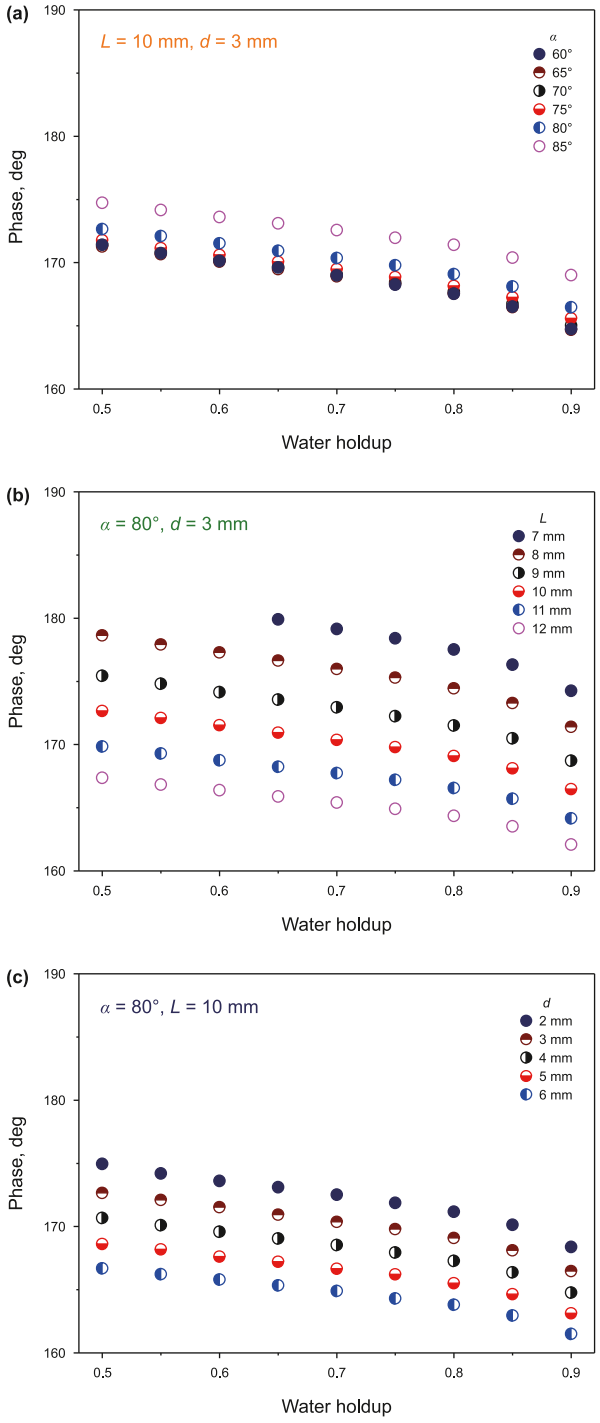

Fig. 7. Phase response of the FMAA versus water holdup (Y_w) for optimized geometric configurations.

$$\tilde{W}_{i,j} = e^{-||x_i - x_j||} \tag{16}$$

This transformation scales the distances to the range [0, 1], where 1 indicates closely neighboring states and 0 represents distant states. The key advantage of this approach lies in eliminating the need to select a recurrence threshold—a parameter that is notoriously difficult to determine optimally (Marwan, 2011). In this study, we adopt a delay time $\tau = 1$, and embedded dimension $m = 2$ for analyzing the weighted recurrence plots (WRPs) of output signals corresponding to four characteristic flow patterns (Fig. 11). The horizontal and vertical axes represent time series points, while the color mapping indicates the weighted recurrence values ($\tilde{W}_{i,j}$). The signals are downsampled to 1 kHz, yielding WRPs for 5-s time series segments.

As illustrated in Fig. 11, the WRP of the D OS/W flow exhibits distinct periodic patterns, with weighted recurrence values ($\tilde{W}_{i,j}$) ranging from 0.1 to 1. This characteristic texture reflects the output signal's pronounced periodic oscillations, which physically correspond to the intermittent formation of oil slugs within the continuous water phase. In the D O/W flow, the WRP exhibits a predominantly stochastic texture pattern, with weighted recurrence values ($\tilde{W}_{i,j}$) concentrated within the range of 0.8–1. This characteristic distribution suggests attenuated signal fluctuations, which physically correspond to the random spatial distribution of polydisperse oil droplets within the continuous phase. In the VFD O/W flow, enhanced turbulent kinetic energy promotes uniform dispersion of micron-scale oil droplets throughout the water phase. This hydrodynamic condition results in significant attenuation of signal fluctuations, leading to the emergence of stochastic texture patterns in the WRP, and the contraction of the $\tilde{W}_{i,j}$ range to [0.95, 1], indicating highly randomized system dynamics. In the TF, the increasing oil fraction results in a significant reduction of the $\tilde{W}_{i,j}$. The alternating occurrence of oil-in-water and water-in-oil flow patterns induces intensified signal fluctuations, causing $\tilde{W}_{i,j}$ to span the entire possible range of [0,1]. The corresponding WRP exhibits a characteristic periodic texture pattern, featuring an alternating arrangement of stochastic scatter points and continuous line segments. These distinct morphological features demonstrate the effectiveness of WRP analysis in identifying and characterizing oil-water flow patterns.

Therefore, the oil-water two-phase flow pattern map in a vertical pipe can be plotted as shown in Fig. 12. The D OS/W flow is appeared in lower water cut and mixture velocity. When the turbulent kinetic energy is large enough, the VFD O/W flow occurs, and the mixture velocity and water cut are both high. When the water cut is lower than 65% at higher mixture velocity, the transition flow appears, which means the flow pattern will develop towards the oil-dominated flows. And the D O/W flow occupies most of the working conditions.

5. Flow parameter prediction in oil-water two-phase flows

5.1. Water holdup measurement

In oil-water two-phase flow systems, variations in water holdup directly influence the mixture's dielectric constant, thereby altering the phase response in microwave measurements. The phase detection circuit employs the AD8302 as its core component, whose operational principle follows the manufacturer-specified relationship between output voltage and phase difference, as expressed by the equation:

$$V_{phas}(V) = -10\ mV/deg \times (|Phase(deg)| - 90\ deg) + 900\ mV \tag{17}$$

The normalized phase output voltage can be calculated as follows:

$$V_w^{nor} = \frac{V_m - V_o}{V_w - V_o} \tag{18}$$

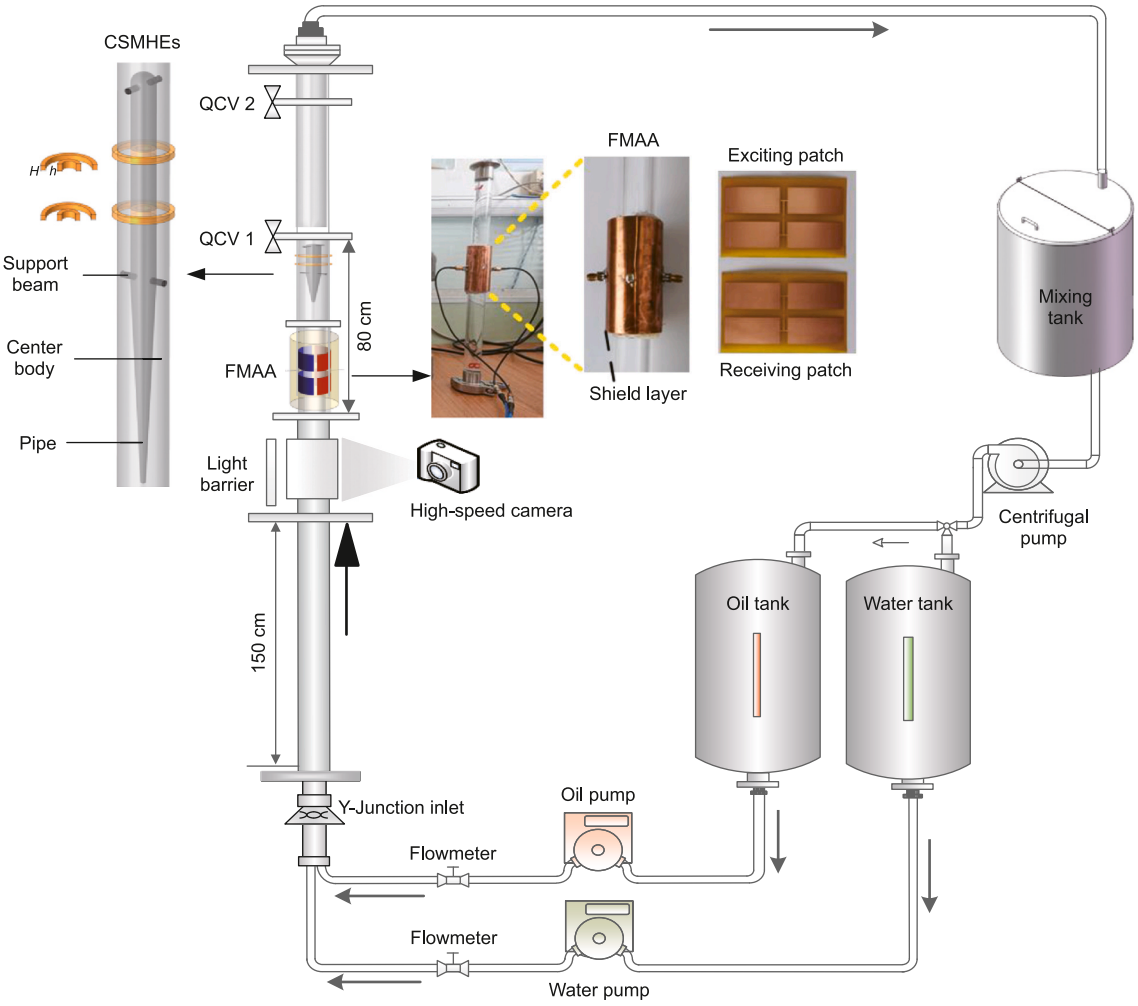

Fig. 8. Schematic of the experimental setup for oil-water two-phase flow characterization.

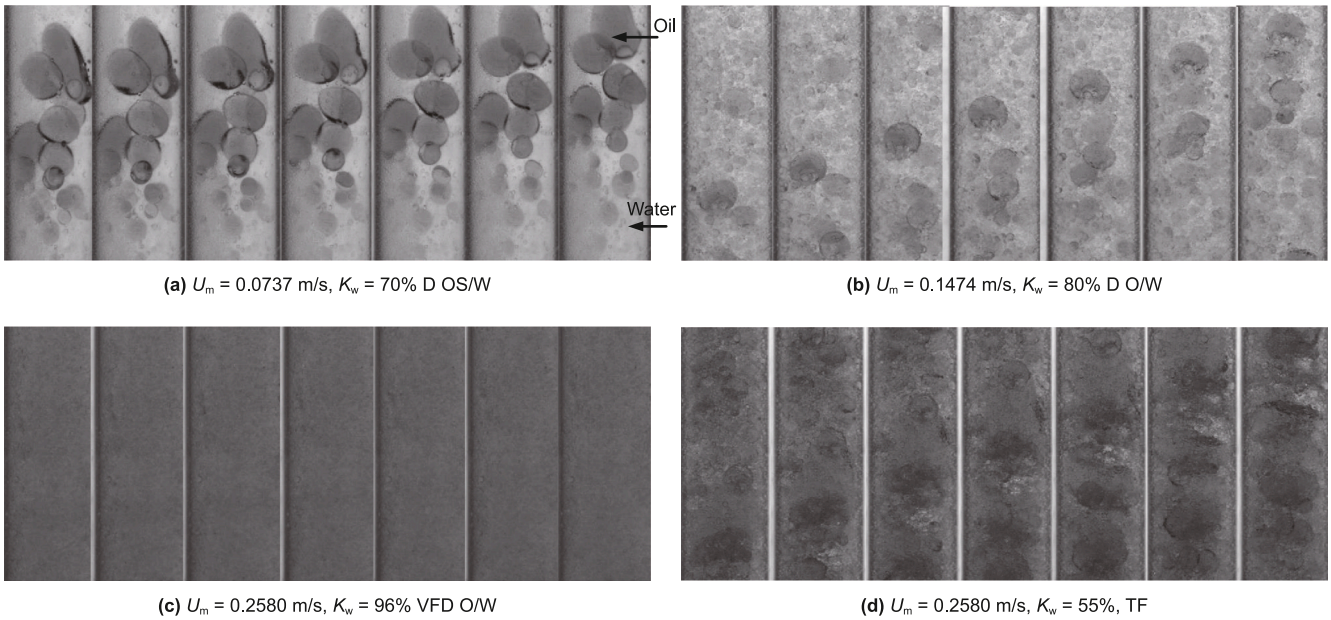

(a) U_m = 0.0737 m/s, K_w = 70% D OS/W

(b) U_m = 0.1474 m/s, K_w = 80% D O/W

(c) U_m = 0.2580 m/s, K_w = 96% VFD O/W

(d) U_m = 0.2580 m/s, K_w = 55%, TF

Fig. 9. Experimental visualization of oil-water two-phase flow patterns in a vertical pipe ($D = 20$ mm).

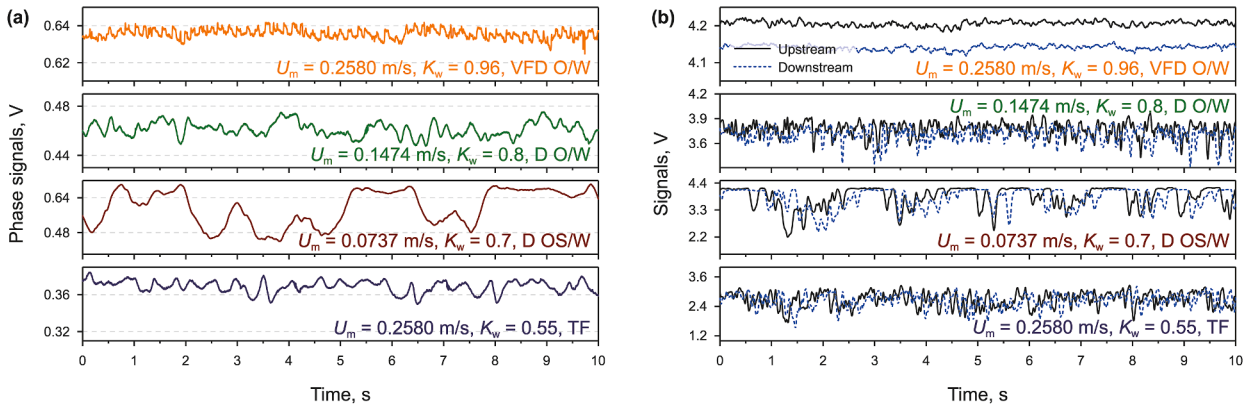

Fig. 10. Synchronized output signals from dual-modality sensors: (**a**) Phase response of the FMAA; (**b**) Conductance fluctuation captured by the CSMHEs.

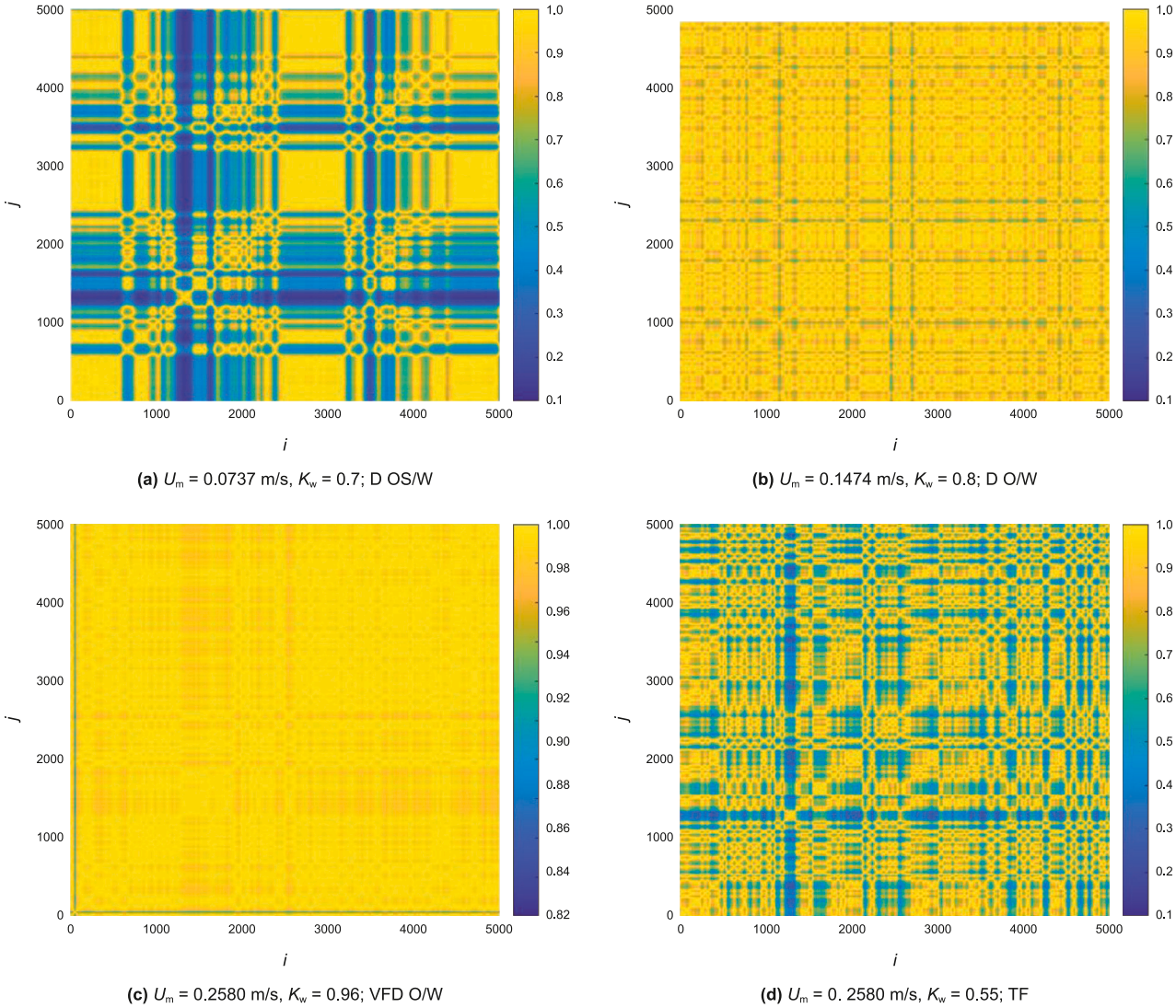

(a) U_m = 0.0737 m/s, K_w = 0.7; D OS/W

(b) U_m = 0.1474 m/s, K_w = 0.8; D O/W

(c) U_m = 0.2580 m/s, K_w = 0.96; VFD O/W

(d) U_m = 0. 2580 m/s, K_w = 0.55; TF

Fig. 11. WRP of conductance sensor signals for four oil-water flow patterns.

where V_w, and V_o are the voltage values at full water and full oil, respectively.

The normalized phase output voltage derived from Eq. (18) is presented in Fig. 13, demonstrating the FMAA's distinctive resolution characteristics. In the high water-cut range (K_w = 80%–98%), where the flow structure remains relatively uniform, the FMAA exhibits superior resolution for differentiating water fractions at elevated mixture velocities (U_m > 0.2 m/s).

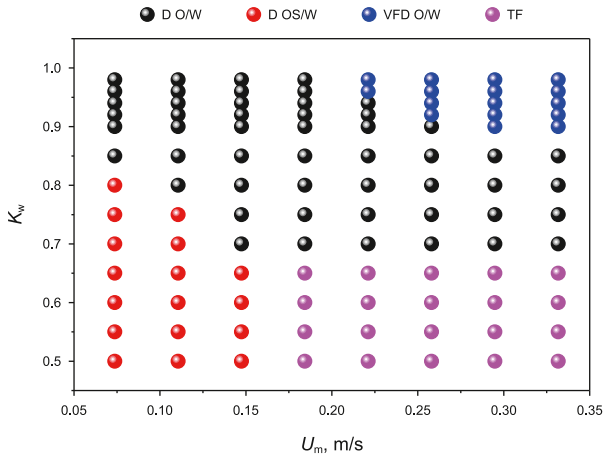

Fig. 12. Flow pattern map for oil-water two-phase flow in a vertical pipe (inner diameter $D = 20$ mm).

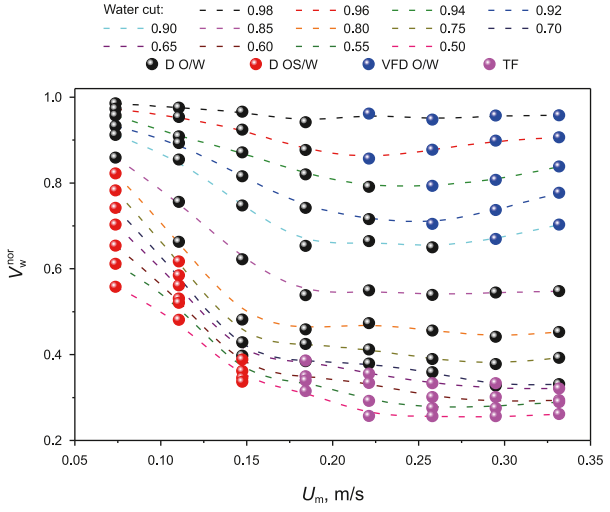

Fig. 13. Normalized phase shift response to variations in U_m and K_w across flow patterns.

Resolution degradation occurs with decreasing K_w due to periodic oil slug passage through the measurement section. Similarly, at low mixture velocities ($U_m < 0.2$ m/s), pronounced phase slippage significantly reduces measurement resolution. Notably, when U_m exceeds 0.2 m/s, the normalized phase output voltage becomes virtually independent of mixture velocity as slippage effects diminish, achieving a sensitivity of 1.45% voltage variation per 1% water-cut change under these stabilized flow conditions.

Based on the response of microwave sensor, the water holdup of vertical oil-water two-phase flow is calculated. In oil-water two-phase flow where water is a continuous phase, significant phase slippage occurs due to density differences and interfacial forces, causing Y_w to consistently exceed the actual K_w. To establish an accurate vertical flow water holdup model, quantitative calibration is performed using QCV measurements. The analysis demonstrates that the flow structure of each flow pattern also varies with changes in water holdup. Hence, a mixed dielectric constant model is developed to represent the oil-water mixing rule, which varies with water holdup:

$$\varepsilon_m^{AY_w+B} = Y_w \varepsilon_w^{AY_w+B} + (1 - Y_w)\varepsilon_o^{AY_w+B} \tag{19}$$

Using the experimental data of the QCV, A and B can be determined. Setting $\gamma = AY_w + B$, γ represents the flow pattern factor. The average value of γ is calculated here as shown in Table 4. Previous research has established that the γ parameter equals -1 when two-phase fluids exhibit series distribution along the electric field direction, while γ becomes 1/3 under random distribution conditions (Lichtenecker and Rother, 1931). Fig. 14 illustrates the FMAA's electric vector distribution in the fluid at the FMAA's central cross-section, showing radially oriented field lines along the pipe. During dynamic experiments, fluids with complex flow structures demonstrate either series or random distributions relative to the electric field direction. By comparing the $\bar{\gamma}$ values corresponding to different flow patterns, it shows that the $\bar{\gamma}$ exhibits values bounded within the interval $[-1, 1/3]$, with the lower bound corresponding to series distributions and the upper bound characterizing random dispersion patterns. And $\bar{\gamma}$ exhibits a gradual increase proportional to the concentration gradient of dispersed-phase oil droplets.

Bring the parameters in Table 4 into Eq. (19) to solve Y_w. Then, we introduce two statistical values, the AAPD (absolute average percentage deviation) and the AAD (absolute average deviation) to evaluate the measurement accuracy:

$$\mathrm{AAPD} = \frac{1}{n}\sum_{i=1}^{n}\frac{\left|Y_i^{pre} - Y_i^{exp}\right|}{Y_i^{exp}} \tag{20}$$

$$\mathrm{AAD} = \frac{1}{n}\sum_{i=1}^{n}\left|Y_i^{pre} - Y_i^{exp}\right| \tag{21}$$

where n is the total working condition number, Y_i^{exp} and Y_i^{pre} are the water holdups of prediction and experiment at i-th working condition.

As can be seen from Fig. 15, the mixed dielectric constant model demonstrates excellent predictive capability for water holdup across all four flow patterns, achieving an AAD of 0.0182 and an AAPD of 2.27%, with overall measurement errors maintained within ±5%. These quantitative results confirm that the FMAA provides reliable and accurate water holdup measurements for diverse flow patterns.

Table 4
Model parameters under four flow patterns.

Flow pattern	A	B	$\bar{\gamma}$
VFD O/W	4.122	−4.017	−0.104
D O/W	0.208	−0.414	−0.225
D OS/W	−0.204	0.206	0.041
TF	−1.485	1.030	0.043

5.2. Cross-correlation velocity measurement

Due to the flow continuity principle, the flow structure observed in the upstream pipe section will propagate to the downstream section after a certain time delay. This flow pattern transmission results in similar fluctuation characteristics appearing in both upstream ($x(t)$) and downstream ($y(t)$) sensor signals with a temporal offset. The time delay between these correlated signals can be quantified through cross-correlation analysis of $x(t)$ and $y(t)$ (Beck, 1981):

$$R_{xy}(\tau) = \lim_{N\to\infty}\frac{1}{N}\int_0^N x(t)y(t+\tau)\mathrm{d}t \tag{22}$$

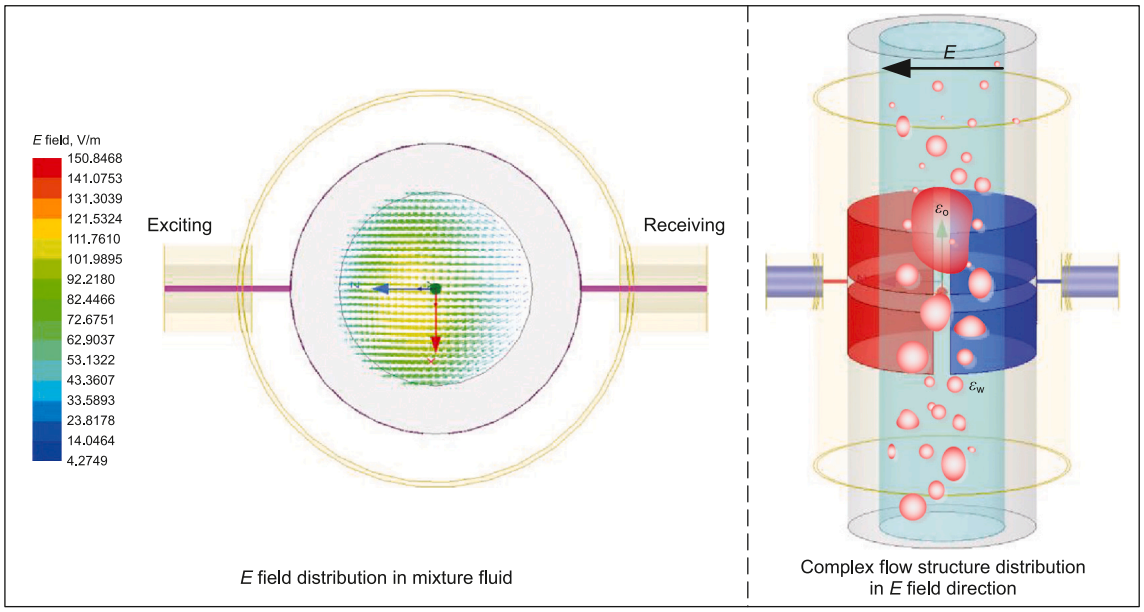

Fig. 14. Electric field vector distribution and orientation in oil-water flow captured by the FMAA.

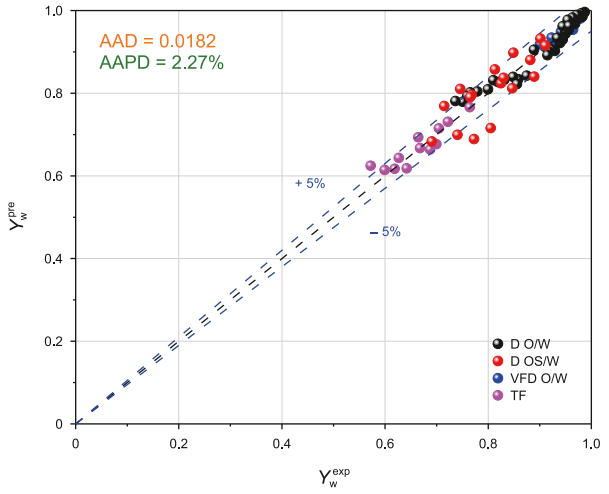

Fig. 15. Prediction results of water holdup in vertical oil-water two-phase flow.

where N is the integration time, and τ_0 is the transit time, which is equal to the τ for max $R_{xy}(\tau)$, so the cross-correlation velocity is solved as: $U_{cc} = l/\tau_0$, where l is the distance from the upper electrodes to the lower of the CSMHEs.

To ensure accurate determination of the U_{cc}, an optimized sampling frequency of 20 kHz was selected based on error propagation analysis (Zhang et al., 2010), effectively constraining the maximum relative measurement error to 0.05%. As illustrated in Fig. 16, the U_{cc} demonstrates excellent waveform preservation during propagation, evidenced by the strong signal correlation between upstream and downstream CSMHEs (Fig. 16(a)). Furthermore, Fig. 16(b) reveals a consistent linear relationship between cross-correlation velocity and mixture velocity at constant water cut, with this correlation remaining invariant across all tested flow patterns—a critical finding that confirms the CSMHEs' capability to reliably capture global structural wave characteristics independent of flow pattern variations.

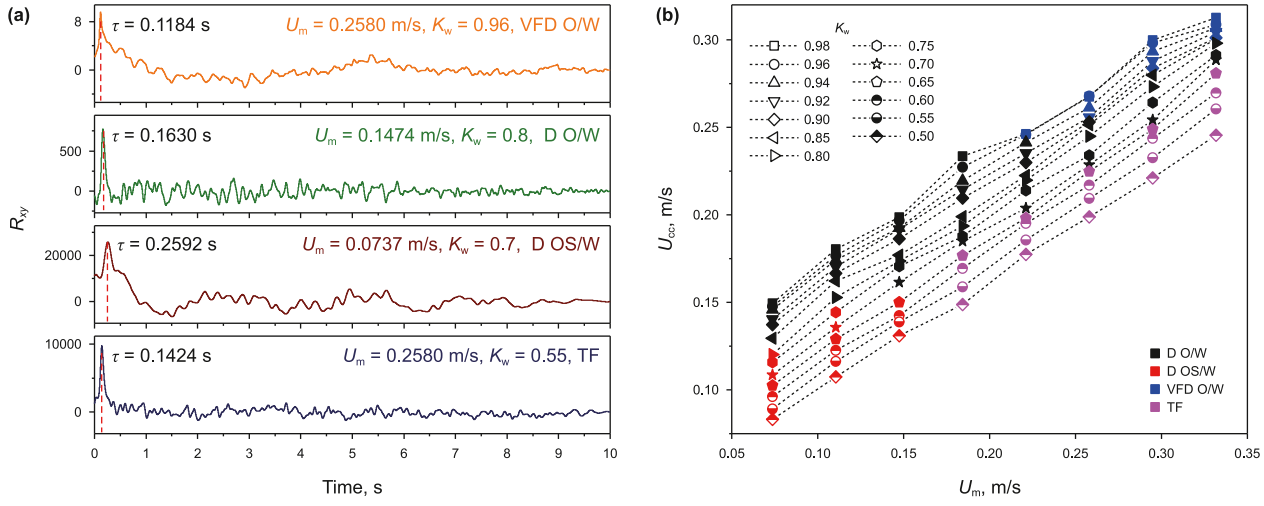

Fig. 16. U_{cc} calculation using CSMHEs: (**a**) Cross-correlation functions for four oil-water flow patterns, (**b**) Relationship between U_{cc}, mixture velocity (U_m), and water cut (K_w).

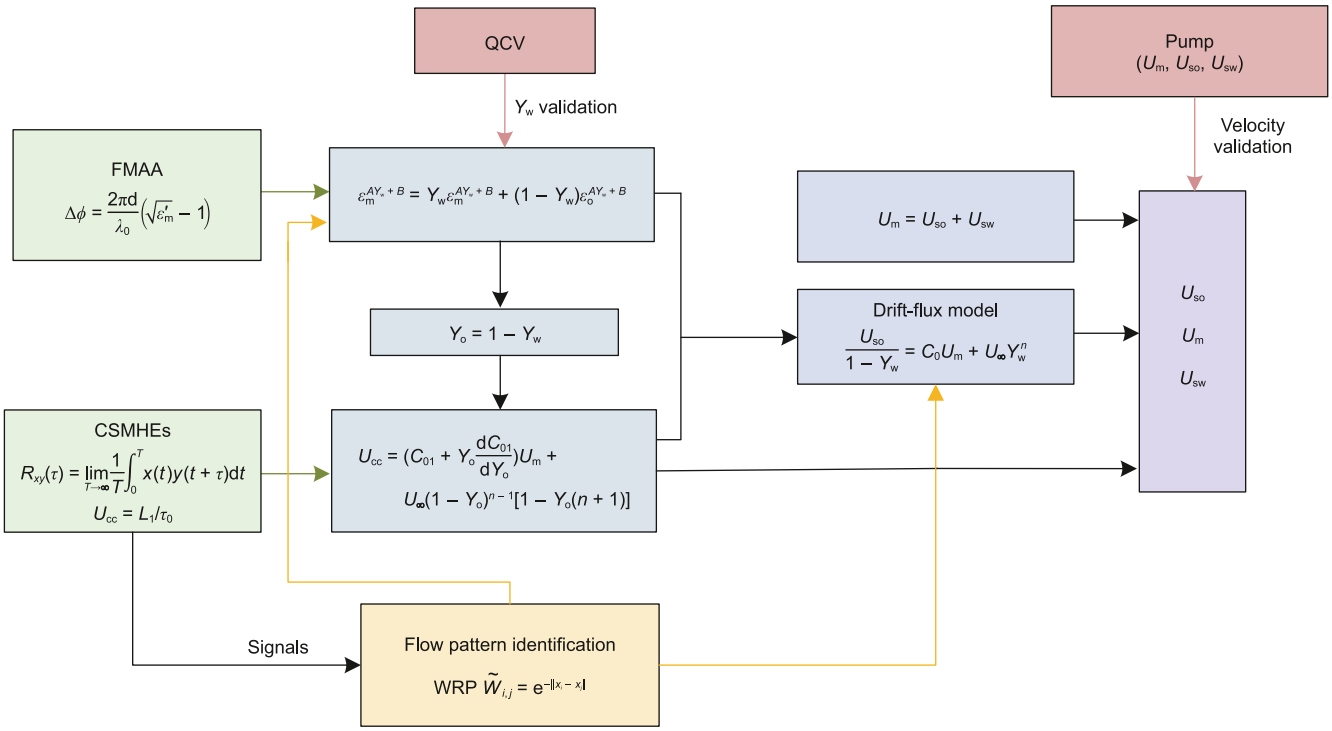

Fig. 17. Flowchart of the flow parameter prediction model.

5.3. Measurement of mixture and superficial velocities

Due to the slippage effect and the interaction between oil and water phases, the U_{cc} is not equal to the U_m. In order to accurately measure the U_m, it is necessary to establish an effective relationship between the U_{cc} and the U_m. Research shows that the kinematic wave velocity U_{kw} is equivalent to the U_{cc} (Kytömaa and Brennen, 1991). Lucas and Jin (2001) found that the variation of the U_{kw} to the U_m is influenced by the dispersed phase distribution and content, there is:

$$U_{kw} = \left(C_{01} + Y_o\frac{dC_{01}}{dY_o}\right)U_m + U_\infty(1 - Y_o)^{n-1}[1 - Y_o(n+1)] \tag{23}$$

where C_0 represents the phase distribution coefficient, n is the droplet size exponent, U_∞ the terminal velocity of a single droplet in infinite still water, Y_o is the oil holdup. Set $C^* = C_{01} + Y_o dC_{01}/dY_o$, $V^* = U_\infty(1 - Y_o)^{n-1}[1 - Y_o(n+1)]$, the relationship between the U_{cc} and the U_m of the oil-water two-phase flow can be expressed as:

$$U_{cc} = C^*U_m + V^* \tag{24}$$

It can be seen that the relationship between the U_{cc} and the U_m is affected by the phase distribution characteristics and the dispersion holdup. Fig. 16(b) shows that the relationship among the U_{cc}, the U_m and the K_w in different flow patterns is close, the C^* and the V^* can be linearly fitted with the K_w:

$$\begin{cases} C^* = a + bK_w \\ V^* = c + dK_w \end{cases} \tag{25}$$

By substituting Eq. (25) into Eq. (24), we get:

$$U_{cc} = (a + bK_w)U_m + c + dK_w \tag{26}$$

By linear fitting, the U_m can be finally obtained:

$$U_{cc} = (0.68712 - 0.04856K_w)U_m + (0.15278K_w - 0.0444) \tag{27}$$

In addition, the water cut of oil-water two-phase flow can be expressed as:

$$K_w = 1 - \frac{U_{so}}{U_m} \tag{28}$$

The superficial velocities of the two phases can be obtained based on the drift-flux model (Zuber and Findlay, 1965) as follows:

$$\frac{U_{so}}{1 - Y_w} = C_0U_m + U_\infty Y_w^n \tag{29}$$

Han et al. (2017) has obtained the modified drift-flux models of the 20 mm-ID vertical oil-water two-phase flow in four flow patterns:

$$\begin{cases} \frac{U_{so}}{1 - Y_w} = 1.00163U_m + 0.11274Y_w^{3.3} \text{ (D O/W\&VFD O/W)} \\ \frac{U_{so}}{1 - Y_w} = 1.36633U_m + 0.05493Y_w^{1.1} \text{ (D OS/W)} \\ \frac{U_{so}}{1 - Y_w} = 1.06556U_m + 0.14827Y_w^{1.5} \text{ (TF)} \end{cases} \tag{30}$$

Substituting the Y_w obtained by the FMAA and the U_{cc} obtained by the CSMHEs into Eq. (30), and combining Eqs. (27), (28) and (30), the mixture velocity, the oil superficial velocity can be obtained. And according to $U_{sw} = U_m - U_{so}$, the prediction result of the

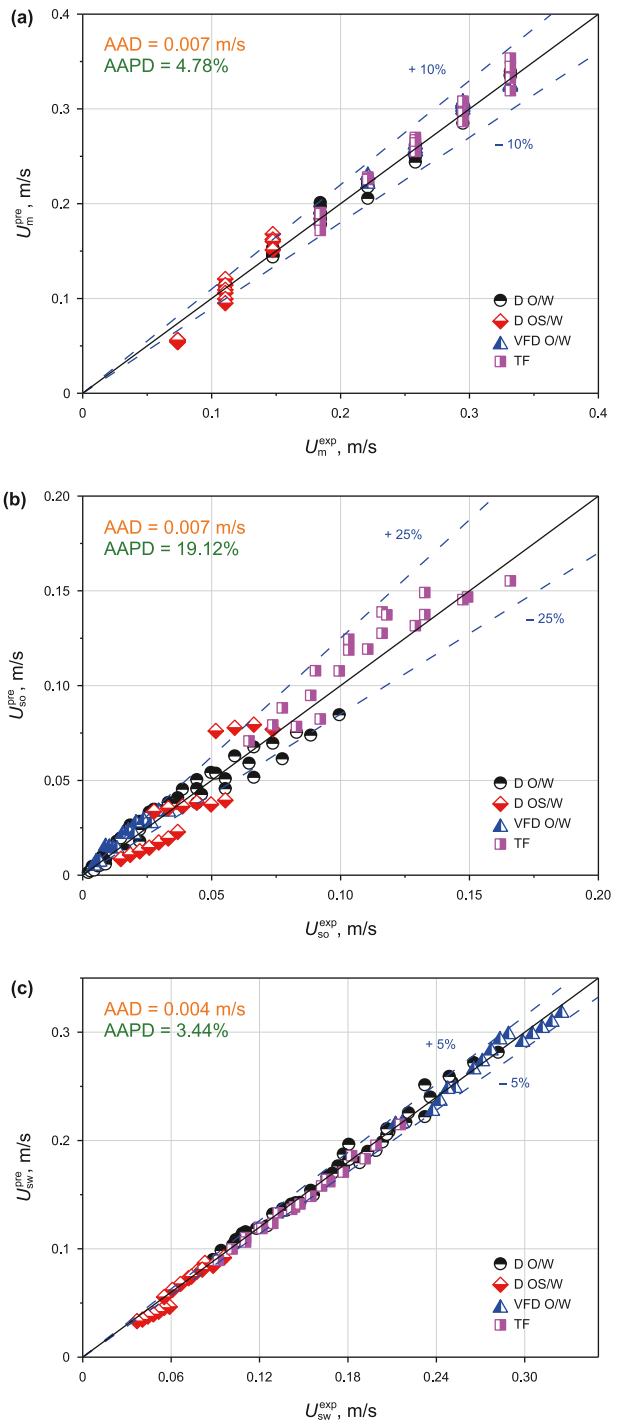

Fig. 18. Prediction results of velocities in oil-water two-phase flow: (**a**) Mixture velocity U_m (m/s); (**b**) Oil superficial velocity U_{so} (m/s); (**c**) Water superficial velocity U_{sw} (m/s).

Table 5
Error metrics for mixture velocity and superficial velocities.

Velocities	Error metrics	D O/W	VFD O/W	D OS/W	TF
U_m	AAD, m/s	0.005	0.006	0.013	0.008
	AAPD	2.44%	2.15%	14.99%	3.22%
U_{so}	AAD, m/s	0.005	0.003	0.011	0.01
	AAPD	18.30%	22.38%	29.19%	9.96%
U_{sw}	AAD, m/s	0.18	0.006	0.004	0.004
	AAPD	0.44%	2.04%	8.02%	2.51%

U_{sw} can be calculated. The complete prediction methodology for these flow parameters is systematically illustrated in the flowchart presented in Fig. 17, which outlines the stepwise computational procedure from raw measurements to final velocity predictions.

Fig. 18 presents the velocity prediction results: For the U_m: All data points falling within the ±10% total error band, supported by the AAD of 0.007 m/s and the AAPD of 4.78%. Due to the flow collecting effect of the center body of the CSMHEs, the mixture velocity in the annular space is larger, the oil phase structure is compressed and deformed, which reduces the flow pattern influence, leading to a high precision. Comparative analysis reveals superior prediction performance for water superficial velocity (U_{sw}) (AAD = 0.004 m/s, AAPD = 3.44%) versus oil superficial velocity (U_{so}) (AAD = 0.007 m/s, AAPD = 19.12%), attributable to the experimental conditions' water-dominated continuous phase (high water cut regime) where the FMAA exhibits optimal measurement accuracy.

U_m and U_{so} are solved simultaneously from a coupled equation system (as shown in Fig. 17), making them mathematically interdependent. However, the high AAPD in U_{so} (19.12%) does not substantially degrade the accuracy of U_m for two key reasons: First, the AAD for U_{so} is only 0.007 m/s, indicating that the absolute prediction error is very small. Second, U_m operates at a much higher velocity magnitude compared with U_{so}. When this small absolute error from U_{so} propagates through the equations to the larger-valued U_m, the resulting relative uncertainty is significantly diluted. The most direct evidence is the final prediction performance: U_m itself achieves a satisfactorily low AAPD of 4.78%. This confirms that the solution process is stable and that the high relative error in U_{so} has not been amplified to a level that critically impacts the mixture velocity prediction.

In addition, we calculate the prediction errors of the mixture velocity (U_m) and the phase superficial velocities under each flow pattern, and the results are shown in Table 5. Notably, both mixture velocity and water superficial velocity demonstrate superior prediction accuracy in bubbly flow patterns (D O/W and VFD O/W), attributable to the FMAA's enhanced resolution in water-dominated systems with randomly dispersed oil droplets and the CSMHEs' effective mitigation of slippage effects. Conversely, oil superficial velocity (U_{so}) predictions exhibit significantly larger errors in bubbly flow patterns due to two compounding factors: (1) the elevated mixture velocities in the CSMHEs' annular space challenge the cross-correlation algorithm's ability to reliably identify correlation peaks from rapidly flowing, finely dispersed oil bubbles; and (2) the inherently low oil holdup under these conditions amplifies relative measurement uncertainties.

The prediction errors of the U_m, the U_{sw}, and the U_{so} are largest in the D OS/W, because of the serious slippage and the large oil slugs leading to the measurement errors of the two sensors. In the TF, the U_{so} has a relatively small error compared with other flow patterns because of large oil content, and the prediction deviation mainly comes from the complex flow structure, oil and water are as continuous phase alternately, the interaction between oil and water is complex.

6. Conclusions

This study presents an innovative dual-modality sensing system combining microstrip and conductivity measurement techniques for oil-water two-phase flow characterization. The FMAA is designed to obtain the water holdup and the CSMHEs designed recently by us is firstly applied to velocity measurement of liquid-liquid flows. The contributions can be summarized as follows:

The FMAA is optimized and simulated using HFSS. Dynamic experiments confirmed that the FMAA is sensitive to water holdup. And the mixed dielectric constant models are established in different flow patterns to predict water holdup. Experimental results demonstrate the FMAA's robust performance across a wide range of operating conditions, achieving exceptional measurement precision with an AAD of 0.0182 m/s and an AAPD of 2.27%.

Due to the multi-height electrode design and the introduction of the center body, the velocity in the annular space of the sensor increases and the influence of slippage is weakened, which improve the prediction accuracy of the cross-correlation velocity. Results indicate the CSMHEs can achieve satisfactory accuracy in liquid-liquid flows.

Combining the water holdup measured by the FMAA, the mixture velocity and the phase superficial velocities under four flow patterns are predicted. The results show that the AAPDs of the mixture velocity and the water superficial velocity are 4.78% and 3.44% respectively. The higher relative prediction error for the oil superficial velocity is attributed to its low velocity magnitude under the medium-to-high water-cut conditions investigated.

The proposed dual-modality system demonstrates significant potential for production logging in high water-cut oil wells, enabling real-time monitoring of dynamic phase distribution and flow patterns to optimize production strategies. Its integration of microwave and conductance techniques provides critical insights into water holdup and velocity profiles, directly addressing challenges such as water breakthrough detection and phase slippage mitigation in mature reservoirs.

CRediT authorship contribution statement

Lan-Di Bai: Writing – original draft, Visualization, Software, Project administration, Investigation, Funding acquisition, Data curation. **Ning-De Jin:** Writing – review & editing, Writing – original draft, Validation, Resources, Project administration, Methodology, Funding acquisition, Data curation, Conceptualization. **Chuan-Shun Liu:** Writing – original draft, Software, Methodology, Investigation, Formal analysis, Data curation. **Ji-Dong Wei:** Visualization, Supervision, Investigation, Formal analysis. **Ying-Yu Ren:** Writing – review & editing, Visualization, Methodology, Investigation, Data curation.

Declaration of competing interest

The authors declare that they have no known competing financial interests or personal relationships that could have appeared to influence the work reported in this paper.

Acknowledgement

This study was supported by the National Natural Science Foundation of China (Grant Nos. 52404035, 42374137), and by the China Postdoctoral Science Foundation (Grant Nos. 2024M762370, 2025T180799).

References

Alvarez, J.O., 2018. Feasibility of a microwave meter for water-cut measurements and permittivity profile. In: IEEE International Symposium on Geoscience and Remote Sensing (IGARSS), pp. 8432–8435. https://doi.org/10.1109/IGARSS.2018.8518426.

Amiri, M., Abolhasan, M., Shariati, N., et al., 2023. RF-self-powered sensor for fully autonomous soil moisture sensing. IEEE Trans. Microw. Theor. Tech. 71 (3), 1374–1387. https://doi.org/10.1109/TMTT.2022.3222222.

Andreussi, P., Donfrancesco, A.D., Messia, M., 1988. An impedance method for the measurement of liquid hold-up in two-phase flow. Int. J. Multiphas. Flow 14 (6), 777–785. https://doi.org/10.1016/0301-9322(88)90074-2.

Asali, J.C., Hanratty, T.J., Andreussi, P., 1985. Interfacial drag and film height for vertical annular flow. AIChE J. 31 (6), 895–902. https://doi.org/10.1002/AIC.690310604.

Bai, L.D., Jin, N.D., Chen, X., et al., 2021. A distributed conductance cross-correlation method for measuring low-velocity and high water-cut oil-water flows. IEEE Sens. J. 21 (21), 23860–23871. https://doi.org/10.1109/JSEN.2021.3115267.

Barnea, D., Shoham, O., Taitel, Y., 1980. Flow pattern characterization for two phase flow by electrical conductance probe. Int. J. Multiphas. Flow 6 (5), 387–397. https://doi.org/10.1016/0301-9322(80)90001-4.

Beck, M.S., 1981. Correlation in instruments: cross correlation flow meters. J. Phys. E 14 (1), 7–19. https://doi.org/10.1088/0022-3735/14/1/001.

Bo, O.L., Nyfors, E., 2002. Application of microwave spectroscopy for the detection of water fraction and water salinity in water-oil-gas pipe flow. J. Non-Cryst. Solids 305 (1–3), 345–353. https://doi.org/10.1016/S0022-3093(02)01130-4.

Bruggeman, D.A.G., 1935. The calculation of various physical constants of heterogeneous substances. I. The dielectric constants and conductivities of mixtures composed of isotropic substances. Ann. Phys. 24, 636–644.

Chen, R.S., Wang, D.X., Yung, E.K.N., et al., 2001. Application of the multifrontal method to the vector FEM for analysis of microwave filters. Microw. Opt. Technol. Lett. 31 (6), 465–470. https://doi.org/10.1002/mop.10064.

Chen, X., Han, Y.F., Ren, Y.Y., et al., 2017. Water holdup measurement of oil-water two-phase flow with low velocity using a coaxial capacitance sensor. Exp. Therm. Fluid Sci. 81, 244–255. https://doi.org/10.1016/j.expthermflusci.2016.10.029.

Costigan, G., Whalley, P.B., 1997. Slug flow regime identification from dynamic void fraction measurements in vertical air-water flows. Int. J. Multiphas. Flow 23 (2), 263–282. https://doi.org/10.1016/S0301-9322(96)00050-X.

Deif, S., Daneshmand, M., 2020. Long array of microwave sensors for real-time coating defect detection. IEEE Trans. Microw. Theor. Tech. 68 (77), 2856–2866. https://doi.org/10.1109/TMTT.2020.2973385.

Demori, M., Ferrari, V., Strazza, D., et al., 2010. A capacitive sensor system for the analysis of two-phase flows of oil and conductive water. Sensor. Actuat. A-phys. 163 (1), 172–179. https://doi.org/10.1016/j.sna.2010.08.018.

Devia, F., Fossa, M., 2003. Design and optimisation of impedance probes for void fraction measurements. Flow Meas. Instrum. 14 (4–5), 139–149. https://doi.org/10.1016/S0955-5986(03)00019-0.

Eckmann, J.P., Kamphorst, S.O., Ruelle, D., 1987. Recurrence plots of dynamical systems. Europhys. Lett. 4 (9), 973–977. https://doi.org/10.1209/0295-5075/4/9/004.

Eroglu, D., Peron, T.K.D.M., Marwan, N., et al., 2014. Entropy of weighted recurrence plots. Phys. Rev. E 90 (4), 042919. https://doi.org/10.1103/PhysRevE.90.042919.

Fossa, M., 1998. Design and performance of a conductance probe for measuring the liquid fraction in two-phase gas-liquid flows. Flow Meas. Instrum. 9 (2), 103–109. https://doi.org/10.1016/S0955-5986(98)00011-9.

Ghretli, M., Khalid, K., Grozescu, I.V., et al., 2007. Dual frequency microstrip antenna sensor for water content measurements independent of temperature variation. Meas. Sci. Technol. 18 (4), 1054–1060. https://doi.org/10.1088/0957-0233/18/4/013.

Gupta, B., Nayak, A.K., Kandar, T.K., et al., 2016. Investigation of air-water two phase flow through a venturi. Exp. Therm. Fluid Sci. 70, 148–154. https://doi.org/10.1016/j.expthermflusci.2015.07.012.

Han, Y.F., Jin, N.D., Zhai, L.S., et al., 2017. Flow pattern and holdup phenomena of low velocity oil-water flows in a vertical upward small diameter pipe. J. Petrol. Sci. Eng. 159, 387–408. https://doi.org/10.1016/j.petrol.2017.09.052.

Hossein, M., Deif, S., Abdolrazzaghi, M., et al., 2018. A microwave ring resonator sensor for early detection of breaches in pipeline coatings. IEEE Trans. Ind. Electron. 65 (2), 1626–1635. https://doi.org/10.1109/TIE.2017.2733449.

Jia, L.L., Zhong, L.G., Li, S.H., et al., 2024. Study of the liquid resistance effect of water-in-oil emulsions in porous media. Pet. Sci. 21, 4165–4175. https://doi.org/10.1016/j.petsci.2024.07.019.

Kamal, B., Vestrum, S., BinDahbag, M.S., et al., 2024. Microwave-enabled chipless sensor for real-time non-contact water-cut measurements. Measurement 228, 114314. https://doi.org/10.1016/j.measurement.2024.114314.

Karimi, M.A., Arsalan, M., Shamim, A., 2018. Design and dynamic characterization of an orientation insensitive microwave water-cut sensor. IEEE Trans. Microw. Theor. Tech. 66 (1), 530–539. https://doi.org/10.1109/TMTT.2017.2708708.

Kestin, J., Sokolov, M., Wakeham, W.A., 1978. Viscosity of liquid water in the range −8 °C to 150 °C. J. Phys. Chem. Ref. Data 7 (3), 941–948. https://doi.org/10.1063/1.555581.

Kongkeaw, P., Srisai, S., Harnsoongnoen, S., 2025. Detection and quantification of water contamination in fuel oil using substrate integrated waveguide resonator-based microwave sensors coupled with multilayer perceptron neural networks. Sensor. Actuat. A-Phys. 384, 116280. https://doi.org/10.1016/j.sna.2025.116280.

Kytömaa, H.K., Brennen, C.E., 1991. Small amplitude kinematic wave propagation in two-component media. Int. J. Multiphas. Flow 17 (1), 13–26. https://doi.org/10.1016/0301-9322(91)90067-D.

Li, D.H., Feng, F.F., Wu, Y.X., et al., 2009. Investigation of the mixture flow rates of oil-water two-phase flow using the turbine flow meter. J. Phys. Conf. 147 (1), 012062. https://doi.org/10.1088/1742-6596/147/1/012062.

Li, Z.C., Lu, T.T., Tsai, H.S., et al., 2006. The trefftz method for solving eigenvalue problems. Eng. Anal. Bound. Elem. 30 (4), 292–308. https://doi.org/10.1016/j.enganabound.2005.10.006.

Lichtenecker, K., Rother, K., 1931. Deduction of the logarithmic mixture law from general principles. Phys. Z. 32, 255–260.

Lin, X.G., Wang, H.Y., Chen, Z., et al., 2020. Measurement of the flow rate of oil and water using microwave and Venturi sensors with end-to-end dual convolutional neural network. Meas. Sens. 10–12, 100018. https://doi.org/10.1016/j.measen.2020.100018.

Liu, C.S., Bai, L.D., Yang, Q.Y., et al., 2022. An improved conductance sensor with inner-outer multi-height ring electrodes for measurement of vertical gas-liquid flow. IEEE Sens. J. 22 (7), 6399–6409. https://doi.org/10.1109/JSEN.2022.3152819.

Lucas, G.P., Cory, J.C., Waterfall, R.C., 2000. A six-electrode local probe for measuring solids velocity and volume fraction profiles in solids-water flows. Meas. Sci. Technol. 11 (10), 1498–1509. https://doi.org/10.1088/0957-0233/11/10/311.

Lucas, G.P., Jin, N.D., 2001. A new kinematic wave model for interpreting cross correlation velocity measurements in vertically upward, bubbly oil-in-water flows. Meas. Sci. Technol. 12 (9), 1538–1545. https://doi.org/10.1088/0957-0233/12/9/321.

Marwan, N., 2011. How to avoid potential pitfalls in recurrence plot based data analysis. Int. J. Bifurcat. Chaos 21 (4), 1003–1017. https://doi.org/10.1142/S0218127411029008.

Olokede, S.S., Deif, S., Daneshmand, M., 2021. Printed concave-like slot for bandwidth enhancement of inset-fed patch antenna on metallic surfaces. Microw. Opt. Technol. Lett. 63, 1745–1752. https://doi.org/10.1002/mop.32815.

Sabzevari, F.M., Winter, R.S.C., Oloumi, D., et al., 2020. A microwave sensing and imaging method for multiphase flow metering of crude oil pipes. IEEE J. Sel. Top. Appl. Earth Obs. Rem. Sens. 13 (99), 1286–1297. https://doi.org/10.1109/JSTARS.2020.2977303.

Sattari, M.A., Hayati, M., 2024. Accurate and non-contact measurement of volume percentages of oil-water f luids using microstrip sensors independent of the volume of sample using artificial neural network. Flow Meas. Instrum. 97, 102621. https://doi.org/10.1016/j.flowmeasinst.2024.102621.

Sheen, J., Hong, Z.W., Su, C.W., et al., 2010. Microwave measurements of dielectric constants by exponential and logarithmic mixture equations. Prog. Electromagn. Res. 100, 13–26. https://doi.org/10.2528/PIER09091706.

Shen, F.Z., Gao, Y., Li, L., et al., 2022. Wideband microwave sensor for downhole water-cut monitoring. IEEE Trans. Geosci. Rem. Sens. 60, 5914512. https://doi.org/10.1109/TGRS.2022.3170650.

Sorocki, J., Piekarz, I., Wincza, K., et al., 2020. Papapolymerou, Broadband microwave microfluidic coupled-line sensor with 3-D-printed channel for industrial applications. IEEE Trans. Microw. Theor. Tech. 68 (7), 2808–2822. https://doi.org/10.1109/TMTT.2020.2972525.

Tang, Z.Y., Jin, N.D., Yang, Q.Y., et al., 2022. Measurement of oil-gas-water flows in vertical pipes using electromagnetic flowmeter and dual-conductance sensors. IEEE Trans. Instrum. Meas. 71, 7501512. https://doi.org/10.1109/TIM.2022.3154002.

Wang, D.Y., Jin, N.D., Ma, J., et al., 2021. Measurement of water holdup in oil-gas-water slug flow using microstrip antenna. IEEE Trans. Instrum. Meas. 70, 8004310. https://doi.org/10.1109/TIM.2021.3096574.

Wang, D.Y., Jin, N.D., Zhai, L.S., et al., 2019. Methodology for production logging in oil-in-water flows under low flow rate and high water-cut conditions. Appl. Geophys. 16 (3), 302–313. https://doi.org/10.1007/s11770-019-0780-3.

Wei, Y., Yu, H.Q., Chen, Q., et al., 2019. Measurement of water holdup in oil-water two-phase flows using coplanar microstrip transmission lines sensor. IEEE Sens. J. 19 (23), 11289–11300. https://doi.org/10.1109/JSEN.2019.2935022.

Xue, Q., Tang, X.C., Li, Y.N., et al., 2020. Contactless and simultaneous measurement of water and acid contaminations in oil using a flexible microstrip sensor. ACS Sens. 5 (1), 171–179. https://doi.org/10.1021/acssensors.9b01965.

Yang, Y.G., Xu, Y., Yuan, C., et al., 2021. Water cut measurement of oil-water two-phase flow in the resonant cavity sensor based on analytical field solution method. Measurement 174, 109078. https://doi.org/10.1016/j.measurement.2021.109078.

Zhai, L.S., Jin, N.D., Zong, Y.B., et al., 2012. The development of a conductance method for measuring liquid holdup in horizontal oil-water two-phase flows. Meas. Sci. Technol. 23 (2), 025304. https://doi.org/10.1088/0957-0233/23/2/025304.

Zhang, W.B., Wang, C., Wang, Y.L., 2010. Parameter selection in cross-correlation-based velocimetry using circular electrostatic sensors. IEEE Trans. Instrum. Meas. 59 (5), 1268–1275. https://doi.org/10.1109/TIM.2010.2040901.

Zhao, C.J., Wu, G.Z., Li, Y., 2019. Measurement of water content of oil-water two-phase flows using dual-frequency microwave method in combination with deep neural network. Measurement 131, 92–99. https://doi.org/10.1016/j.measurement.2018.08.028.

Zuber, N., Findlay, J.A., 1965. Average volumetric concentration in two-phase flow systems. J. Heat Tran. 87 (4), 453–468. https://doi.org/10.1115/1.3689137.